Orientation Matters: Learning Radiation Patterns in Multi-Rotor UAVs

NON-ARCHIVAL! Redacted for the Conn. Auton. Rob. Sys. Workshop @ ICRA 2026. Full paper under review.

Martin Zoula[1], Daniel Bonilla Licea[2], Jan Faigl[1], Václav Navrátil[1], Martin Saska[1]

***Abstract*— The paper presents learning antenna Radiation Patterns (RPs) in a pair of heterogeneous quadrotor Uncrewed Aerial Vehicles (UAVs) from calibration flight data. RPs are modeled either as a Spherical Harmonics series or as a weighted average over inducing samples. Linear regression of polynomial coefficients simultaneously decouples the two independent UAVs' RPs. A joint calibration trajectory exploits available flight time in an obstacle-free anechoic altitude. Evaluation on a real-world dataset demonstrates the feasibility of learning both radiation patterns, achieving 3.6 dB RMS error—the measurement noise level. The proposed RP learning and decoupling can be exploited for rapid recalibration upon payload changes, autonomous path planning, and swarm control.**

I. Introduction

Communication awareness exploits a model of communication quality for the benefit of a robotic mission. However, field robots lack precise knowledge of environmental physical properties (such as permittivity or permeability) and have only limited computational power. Thus, rigorous models such as electromagnetic field solvers or ray tracing are degraded in the assessment of onboard communication availability; surrogate simlified models are sought.

Contemporary robotic research focuses on modeling signal attenuation in specific environments [1] or end-to-end channel modeling [2]. However, the Radiation Pattern (RP) variations can incur up to $-20\,\mathrm{dB}$ attenuation [3]. E.g., see Fig. 1 depicting $-10\,\mathrm{dB}$ direction-dependent yield in our Uncrewed Aerial Vehicles (UAVs). Albeit an established research topic in telecommunications, mobile robotics so far consider RPs only theoretically [4] or with a fixed pre-identified RP model.

We explore and compare several Radiation Pattern models in the Friis transmission equation, adequate for UAVs in obstacle-free space [5],

$$\underbrace{P_{rx} = P_{tx}}_{\text{sig. power}} + \underbrace{G_{rx} + G_{tx}}_{\text{antenna gains } \mathcal{G}} + \underbrace{20\log_{10}\frac{\lambda}{4\pi d}}_{\text{path loss}}. \tag{1}$$

P are signal powers in dB, $\mathcal{G} = G_{tx} + G_{rx}$ are attenuations caused by (mis)aligned antenna RPs, d is the Euclidean distance between radios, and λ is wavelength. The presented methods decouple the joint $\mathcal{G}$ into two independent RP terms, G_{tx} and G_{rx}, learnt from a specific calibration flight. Specifically, we represent G using either a Spherical Harmonics series or a Basis Grid weighted interpolation.

[1]Authors are with the Faculty of Electrical Engineering, Czech Technical University in Prague, {zoulamar|faiglj|navrava2|saskam1}@fel.cvut.cz

[2]Daniel Bonilla Licea is with the Mohammed VI Polytechnic University, Morocco, daniel.bonilla@um6p.ma

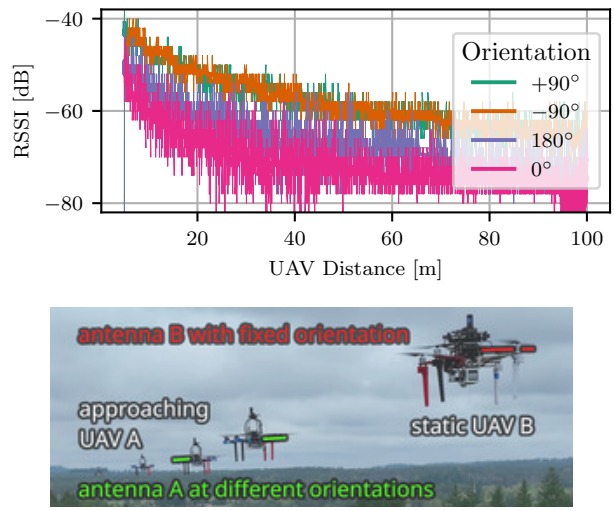

Fig. 1. Illustration of our work. UAV A approaches UAV B four times; each time, however, attaining a different relative antenna orientation. Both antennas were always horizontal, parallel to the ground. However, antenna A bore a different heading on each approach. As apparent from the recorded Received Signal Strength Indicator (RSSI), choosing an appropriate orientation leads to consistent signal strength gain of around 10 dB.

The models were evaluated on a dataset captured during real-world outdoor flight, using off-the-shelf 2.4 GHz radio. The prediction RMS error was as low as 3.6 dB—the inherent measurement noise, with 95 % test errors under 7.5 dB. The spherical harmonics performed the best; model overfitting in higher-order models is also discussed. The paper thus contributes (i.) a practical method to learn and decouple *both* UAV Radiation Patterns simultaneously and (ii.) a fast trajectory suitable for learning the RPs in the field, e.g., after payload change.

II. Background

Communication-aware robotics entail link-layer, network-layer, and spatial models, combined with navigation and networking algorithms [6,7]. In the following text, we focus only on link-layer modeling. Generally, the received signal power P_{rx} can be computed by numerical solutions of the Maxwell equations or by ray tracing [8], if given a precise model of the robot and the environment. However, field robots lack such models.

Surrogate models such as statistical [9] or machine-learning [2,10] can provide signal quality estimates based on imperfect environmental percepts. Precise predictions are possible in a known environment [11] and environmental feature regression is useful in ground robots [1]. In air-to-ground scenarios, scattering and multipath or ground reflec-

tions become significant [12]. Proper models can facilitate dynamic UAV localization [13] or calibrate an experimental antenna array [14].

In UAV air-to-air channel, the airframe shadowing become significant [3,4]. Although directivity can be dynamically controlled by an antenna array [15], our work focuses on transceivers with a single static antenna. To the best of our knowledge, communication-aware robotics has so far considered only pre-identified directional gain (Radiation Pattern) in theory at best, although beneficial in, e.g., transmission security [16,17] or for airborne relay efficiency [4]. Our paper extends prior work with a method for learning UAV Radiation Patterns in practical scenarios.

We regard the work of Matson et al. [18] as the most similar; a measuring UAV samples a sphere around a UAV hovering in obstacle-free (anechoic) altitude, enumerating the effect of polarization on the attainable bit rate. We extend their work with a more generic formulation based on signal power attenuation, enabling the identification of *both* Radiation Patterns and proposing a faster identification trajectory. Besides, a recent preprint proposed learning of the joint air-to-ground directional gain with fixed UAV heading [19].

A. Communication Directivity and Radiation Patterns

All real-world radio systems are inherently direction-dependent and exhibit non-trivial RP. Recalling Eq. (1),

$$G_a \sim G_a(\alpha_b^a, \beta_b^a), \tag{2}$$

where α_b^a and β_b^a are azimuth and inclination angles of the remote UAV b antenna with respect to (w.r.t.) the local reference frame of UAV a antenna. Considering an ideal antenna, however, is naive. In practice, both the UAV airframe (fuselage) and payload interfere with the radiated electromagnetic field and further distort the RP of the antenna. The overall UAV-with-antenna system shall be regarded as a single complex antenna that can pose a significant attenuation dependent on the Angle of Incidence (AoI) in the far field [3,20,21]. See Fig. 2 for illustration.

Antenna RPs are commonly modeled using an electromagnetic field numerical solver or measured in an anechoic chamber. Although methods to reconstruct the "full 3D" pattern from the principal cuts exist [22], complex UAVs may generate main lobes and nulls outside of the two cuts, and the assumption $G = f(G^a(\alpha), G^i(\beta))$ may not necessarily hold. Several approaches were already devised to model the "full 3D" pattern. Goniometric functions [23] or adjusted harmonic series [24] allow reasoning about antenna placement [25].

B. Modular Under-Actuated UAVs

We assume a simplified model of a multi-rotor UAV. State of an UAV u in time t is observed as $\mathcal{S}_u(t) = [x_u(t), y_u(t), z_u(t), \phi_u(t), \theta_u(t), \psi_u(t)]^\intercal$, where x, y, and z are Euclidean coordinates and ϕ, θ and ψ are rotations about respective axes in a global origin frame. UAVs are, however, considered non-holonomic (not omnidirectional), allowing quasi-static control only in reduced state space $\hat{\mathcal{S}}_u(t) = [\hat{x}_u(t), \hat{y}_u(t), \hat{z}_u(t), \hat{\psi}_u(t)]^\intercal$, where the rotation ψ about z-axis is the UAV heading [26]. See the illustrative Fig. 2. The UAV is assumed to keep its properties during a single flight, but may undergo repairs, payload change, or other modifications between flights. Thus the need for rapid RP re-identification.

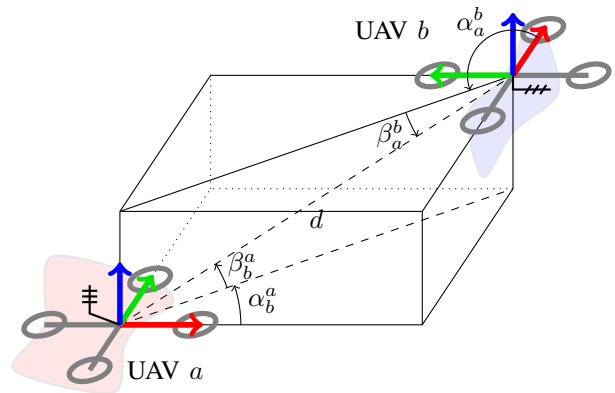

Fig. 2. Radiation pattern geometry. Two UAVs see each other at independent azimuths α_b^a and α_a^b. Although inclinations β_b^a and β_a^b are opposite due to UAV non-holonomy, we still consider both. Pairs of angles α, β comprise the respective Angle of Incidence. Each UAV has an antenna affixed somewhere near its local reference frame origin; together with the UAV structure, each UAV-with-antenna system becomes a complex antenna. The patterns are illustrated as red and blue blobs.

III. Problem Statement

We are interested in fast, practical, infrastructure-free radiation pattern identification for modular, non-holonomic UAV systems. Formally, given a pair of UAVs a and b in an obstacle-free environment, we measure the transmitted and received power $\boldsymbol{P_a}$ and $\boldsymbol{P_b}$ in dB, at observed joint position $\boldsymbol{\mathcal{S}_{a,b}} = (\boldsymbol{\mathcal{S}_a}, \boldsymbol{\mathcal{S}_b})$ of both UAVs. In the notation used, the bold symbols denote matrices whose entries are samples from the respective continuous-time quantities.

We are provided with a dataset $\boldsymbol{P_{rx}} = \boldsymbol{P_{tx}} + \mathcal{G}(\boldsymbol{\mathcal{S}_{tx,rx}}) + 20\log_{10}\frac{\lambda}{4\pi \boldsymbol{d}}$, where $\mathcal{G}$ is the joint coupled Radiation Pattern of both UAVs and $tx \neq rx;\ tx, rx \in \{a, b\}$. The task is to find (i) a joint trajectory $\hat{\mathcal{S}}_{a,b}(t)$ to provide useful training samples, (ii) a learning scheme to decouple $\mathcal{G}(\boldsymbol{\mathcal{S}_{tx,rx}})$ into $G_{rx}(\boldsymbol{\alpha_{tx}^{rx}}, \boldsymbol{\beta_{tx}^{rx}}) + G_{tx}(\boldsymbol{\alpha_{rx}^{tx}}, \boldsymbol{\beta_{rx}^{tx}})$, and (iii) a particular G model under the following assumptions.

1) Wave polarization is neglected.
2) The UAV-antenna origin is the respective UAV origin.
3) The radio channel is reciprocal.
4) The channel is fixed and free of interference.
5) Radios operate in the far field.
6) Propeller blade scattering [21] is neglected.
7) UAVs and their antennas can be different.

IV. Proposed Method

A. Joint UAV Trajectory for Radiation Patterns Learning

Whereas cheap and robust, multi-rotor UAVs cannot maintain an arbitrary 6-Degrees of Freedom (DoF) pose. That

is why we cannot directly replicate the anechoic chamber midair, where one UAV would loiter in place, and the other would twist in place to cover all the directions. Instead, we designed a trajectory that covers all relative orientations of the radios as follows. Both UAVs begin $d = 10\,\mathrm{m}$ away in an initial height $z_0 = 20\,\mathrm{m}$, high enough to consider ground reflections negligible. Then, both UAVs start flying around a vertical circle of a constant diameter d, centered directly between the UAVs. After each loop, one of the UAVs changes its heading angle, such that after the trajectory is complete, both UAVs would have sampled full 360°. See Fig. 4b. While executing the trajectory, we can match the measured signal strengths $P_a(t), P_b(t)$ with the observed joint pose $\mathcal{S}_{a,b}(t)$ of both UAVs at given time t. Obtaining $\boldsymbol{P_a}, \boldsymbol{P_b}, \boldsymbol{\mathcal{S}_{a,b}}$, we can focus on the learning itself.

B. Radiation Patterns Learning

Learning (identification) of RPs from signal samples collected along the learning trajectory involves decoupling the joint attenuation $\mathcal{G}$ into independent components $G_a + G_b$. Following the assumption 1), the methods require transforming the observed joint 12-DoF state $\mathcal{S}_{a,b}$ into α-β form as

$$\alpha_b^a = \arctan(y_b^a, x_b^a), \quad \beta_b^a = \arctan(z_b^a, \|(x_b^a, y_b^a)\|), \quad (3)$$

where $\arctan$ is sign-aware arc tangens and $\circ_a^b$ denotes a quantity transformed w.r.t. frame of reference b. See Fig. 2. Thus, the learning is the residual-minimization task

$$(\phi, \psi)* = \underset{\phi,\psi}{\arg\min} -\boldsymbol{P_{rx}} + \boldsymbol{P_{tx}} + \\ + G_a(\boldsymbol{\alpha_b^a}, \boldsymbol{\beta_b^a}; \boldsymbol{\phi}) + G_b(\boldsymbol{\alpha_a^b}, \boldsymbol{\beta_a^b}; \boldsymbol{\psi}) + 20\log_{10}\frac{\lambda}{4\pi \boldsymbol{d}}, \quad (4)$$

where the same RP model class G is used for both UAVs, however, each with an independent learnable set of free latent parameters $\boldsymbol{\phi}$ and $\boldsymbol{\psi}$ respectively.

In the following paragraphs, we present the three considered radiation pattern models, the Spherical Harmonics (SH), Basis Grid (BG), and Polynomial (P). All of them are functions linear in learnable parameters, i.e.,

$$G_a, G_b \sim \sum_i p_i f_i(\alpha, \beta), \quad i \in \phi \text{ or } \psi.$$

Latent parameters p_* are thus solutions of an ordinary overdetermined linear least squares problem. However, decomposing $\mathcal{G}$ can yield an infinite number of models $\mathcal{G} = G_1 + \varepsilon + G_2 - \varepsilon$, as ε included in the parameters can be arbitrary. That is why we used ridge regression with an empirically tuned hyperparameter, $\kappa = 50$, to regularize the parameters and eliminate ε.

C. The Spherical Harmonics (SH) Model

Let us assume the radiation pattern G is a scalar function defined on a sphere over two polar variables α, β. Such a function may be expressed in terms of an orthogonal polynomial system, e.g., Legendre polynomials. The scalar

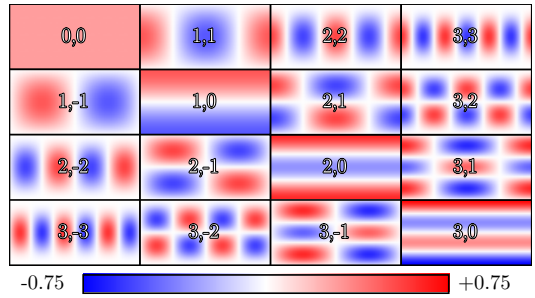

Fig. 3. Illustration of the SH basis functions, $l \in \{0, 1, 2, 3\}$. Horizontal (x) axes denote azimuth, vertical (y) axes denote inclination.

spherical harmonics comprise a series of regularized Legendre polynomials, already proven as a suitable tool in radiation pattern modeling [27]. It reads as

$$G(\alpha, \beta; \boldsymbol{p}) = \sum_{l,m} p_{l,m} Y_{l,m}, \quad Y_{l,m} = \\ \begin{cases} -1^m \sqrt{2\frac{2l+1(l-|m|)!}{4\pi(l+|m|)!}} \mathcal{P}_l^{|m|}(\cos\alpha)\sin(|m|\beta), & m < 0 \\ \sqrt{\frac{2l+1(l-|m|)!}{4\pi(l+|m|)!}} \mathcal{P}_l^m(\cos\alpha), & m = 0 \\ -1^m \sqrt{2\frac{2l+1(l-m)!}{4\pi(l+m)!}} \mathcal{P}_l^m(\cos\alpha)\sin(|m|\beta), & m > 0. \end{cases} \quad (5)$$

where $\mathcal{P}$ is the associated Legendre polynomial. See Fig. 3 with an illustration of several initial functions of the function system. We use spherical harmonics to our advantage, as they are a convenient tool compatible with our learning scheme.

D. The Basis Grid (BG) Model

We also investigated a "primary-domain" approach, as opposed to "dual-domain" described above in the SH method. (An analogy might be seen in the Fourier time and frequency domains.) The BG samples the azimuth-inclination domain for both RP terms; each such sample represents a single regression parameter, locally contributing to the total gain in the queried direction. Formally,

$$G(\alpha, \beta; \boldsymbol{p}) = \sum_{i,j} p_{i,j} \mathcal{K}(\alpha, \beta, i, j), \quad (6)$$

where $\mathcal{K}$ is a kernel function over points on the unit sphere

$$\mathcal{K}(\alpha, \beta, i, j) = \exp\left(\frac{-\|(\alpha, \beta), (i, j)\|^A}{2\sigma}\right), \quad (7)$$

$i \in \langle -\pi, \pi \rangle, j \in \left\langle \frac{-\pi}{2}, \frac{\pi}{2} \right\rangle$, σ is a length-scale hyperparameter, and $\| \circ \|^A$ is angular distance between points on sphere defined by angles (α, β) and (i, j), respectively. Each parameter $p_{i,j}$ represents a point on a sphere defined by azimuth-inclination angles i, j.

E. The Polynomial (P) Model

For the sake of completeness, we also investigate an unconstrained polynomial model over the azimuth and inclination input variables, although it does not reflect the periodicity of its domain.

$$G(\alpha, \beta; \boldsymbol{p}) = \sum_{\boldsymbol{k}} p_{\boldsymbol{k}} \mathcal{B}(\alpha, \beta; \boldsymbol{k}), \quad (8)$$

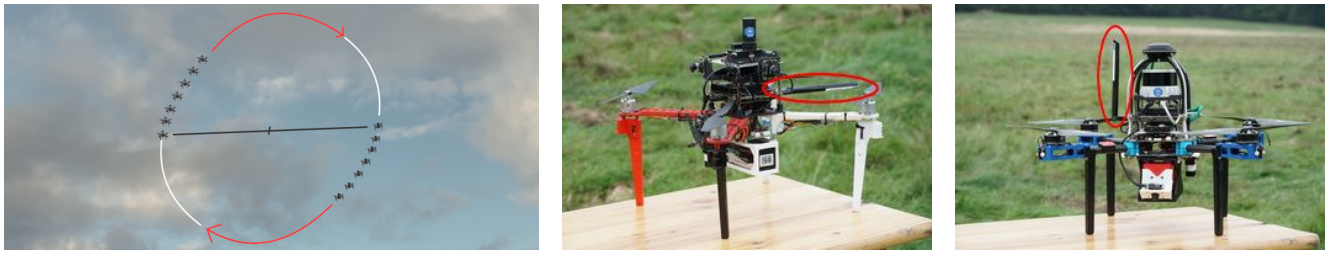

(a) Footage from the calibration flight execution. UAVs circle around each other, and after each loop, one UAV slightly changes its heading. Nearest obstacle is over 50 m away.

(b) `DJI F450` UAV with `T2U` antenna (circled) in horizontal position. Ultraviolet Detection and Ranging (UVDAR) payload attached.

(c) `Holybro X-500` UAV with `T2U` antenna in vertical position. Light Detection and Ranging (LiDAR) payload attached.

Fig. 4. Used UAV platforms and the experimental venue.

where $\mathcal{B}$ yields all possible polynomials over α, β up to requested order as encoded in k.

V. Results

A. Baseline Models

The selected baseline models are the Mean (M) and the Nearest Neighbor (NN) regressions. The former uses the entire training set to compute a mean output value regardless of the feature vectors. Although uninformed, it served as an upper bound on prediction error. The latter weights values corresponding to k nearest neighbours in the observed joint feature space $\boldsymbol{\mathcal{S}}_{a,b}$ w.r.t. the Euclidean distance in the feature space, i.e., Nearest Neighbor (NN) learns the joint RP as in [19]. Baselines are, however, unable to decouple the joint Radiation Pattern $\mathcal{G}$ into $G_a + G_b$.

B. Experimental Setup

1) Venue: The data were collected in an open, slightly sloped field in a rural area depicted in Fig. 4a.

2) UAV Platforms: We used quadcopter UAVs with the `DJI F450` and `Holybro X500 V2` frames with `Holybro Pixhawk 4` and `6X`, respectively, both with `Holybro H-RTK F9P GNSS` module. See Figs. 4b to 4c. Onboard `Intel NUC10i7FNH/K` ran the `ROS Noetic` middleware for flight control and recording.

3) Radio: The Received Signal Strength Indicator (RSSI) was recorded by an off-the-shelf lightweight `TP Link Archer T2U Plus` Wi-Fi USB module, which supports reading the RSSI via so-called "monitor mode." Both devices exchanged frequent (up to 400 Hz) packets, each annotated with the implicitly known transmitted power (20 dBm) and the received power reported as RSSI. However, neither radio was calibrated. The measured values might be inconsistent between flights, but should be consistent during a single short flight. In addition, preliminary tests indicated significant nonreciprocity in the radio system. Although the antennas are reciprocal in the far field, uncalibrated signal processing electronics introduce slack of up to several dB between $a \to b$ and $b \to a$ channels. Hence, we limited the learning and evaluation to a single direction.

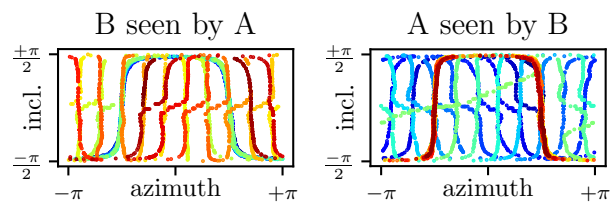

(a) Mutual relative bearing of both UAVs as azimuth-inclination plots, captured during the calibration trajectory; see Section IV-A and Eq. (3).

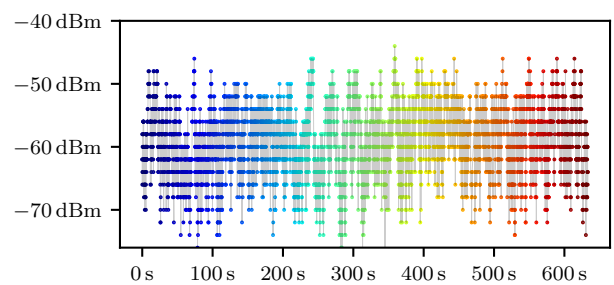

(b) Raw signal strength recorded during the flight.

Fig. 5. Illustration of the representative dataset. Plots Figs. 5a and 5b share the same time base. Color denotes the timestamp; points with matching color represent the same dataset point. The figures depict a legible subsampled version of the original dataset. The original dataset has 27 958 samples.

4) Pose-Signal Sample Matching: Based on the signal sample timestamps, the corresponding poses of both vehicles were interpolated from the recorded trajectory. The `chrony`[1] Network Time Protocol (NTP) implementation was selected for clock synchronization for its sub-millisecond accuracy.

C. Evaluation of Radiation Pattern Models

Out of several, we present a single representative flight. The entire real-world calibration trajectory, illustrated in Fig. 4b, was sampled with 27 958 localized RSSI samples. See Fig. 5 for dataset details. After the flights, the data were subjected to a randomized cross-validation scheme. In 30 instances, all signal samples were split into 80 % training set and 20 % testing set. Test samples were used

[1] `https://gitlab.com/chrony/chrony`

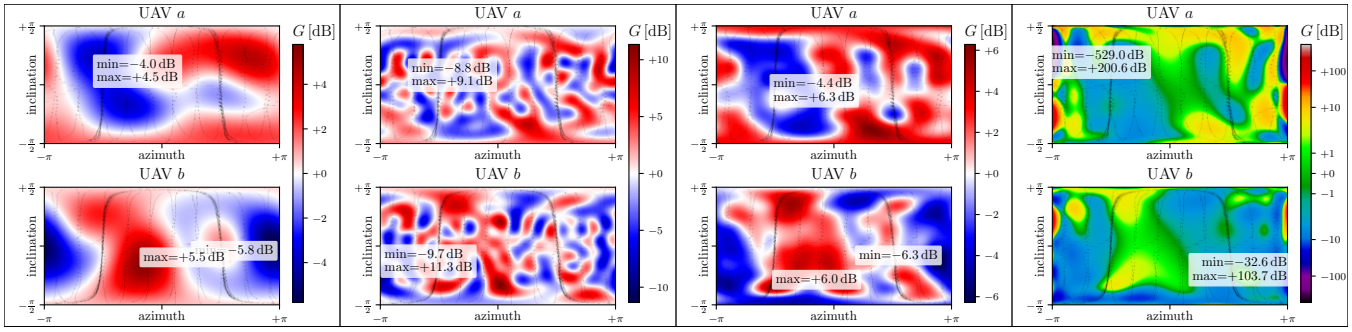

(a) Spherical Harmonics (SH), order 4. (b) SH, order 14. (c) Basis Grid (BG), order 10. (d) Polynomial (P), ord. 19, log. scale.

Fig. 6. A learnt radiation patterns selection. The sub-figures pairs depict both decoupled RPs G_a and G_b in the α-β domain. Black points represent the samples, same as in Fig. 5a. The dense sampling at UAV A's azimuth $\alpha \approx \pm\frac{\pi}{2}$ corresponds to the sparse sampling on UAV B and vice versa.

to evaluate prediction error using Root-Mean-Squared-Error (RMS) and Akaike Information Criterion (AIC). Further, a rough estimate of computational demands is included as Linearized Time Demand (LTD), which is the total CPU time required for learning, as implemented in Python's `time.perf_counter`. Finally, we include the absolute errors 95th Quantile (Q95).

The naive baseline Mean (M) method provided an upper bound on prediction accuracy of $5.43\,\text{dB}$ RMS. As proposed methods exploit observed variables $\alpha_a^b, \beta_a^b, \alpha_b^a, \beta_b^a$, and d, their RMS should decrease. Contrarily, the 10-neighbor NN provided a hint on the best possible prediction of $3.43\,\text{dB}$ RMS; predicting the joint RP $\mathcal{G}$ (as in [19]) was unconstrained by a specific model, but all training samples served as parameters. The UAVs radiation pattern was measured in an anechoic chamber for reference; the signal strength differed by up to $10\,\text{dB}$ in the azimuthal (horizontal) plane and up to $20\,\text{dB}$ in the inclination (vertical) plane.

Proposed models were examined with various parameter count $|\phi|$, related to the highest order of Legendre polynomial in the SH or the number of inducing samples in the BG. Evaluation of representative variants with $|\phi| \approx 200$ is presented in Table I. The learned radiation patterns are illustrated in Fig. 6. The SH method (Fig. 6b) emerged as the most promising. Increasing the model complexity enabled finer-grained Radiation Pattern learning as depicted in Figs. 6a and 6b. It can be observed that RMS and AIC values surpassed those of other methods, although more demanding to compute depending on the implementation. The BG (Fig. 6c, $\sigma = 0.03$) exhibited worse. Further hyperparameter tuning could make it equal with SH, as only a rough grid search was employed for the initial evaluation presented here. Finally, according to Fig. 6d, the P method is confirmed less useful, as it ignores the domain periodicity; despite, its performance matched the BG.

Figure 7 depicts SH method with quite a high Legendre polynomial order of 28 and parameter count $|\phi| = 784$. It is questionable whether overfitting occurred. The parametrization exhibited the best AIC score, suggesting that all parameters still contributed to learning the underlying radiation pattern rather than random noise. Accordingly, all

TABLE I

PERFORMANCE COMPARISON OF SELECTED METHODS.

Method	RMS [dB]	$\lvert\phi\rvert$ [-]	AIC $\cdot 10^{-3}$ [-]	LTD [s]	Q95 [dB]
M	5.43	1	25.06	0.0001	10.93
NN-10	3.43	22,367	21.05	0.0081	7.09
SH-4	4.64	16	23.30	0.0054	8.95
SH-14	3.73	196	20.87	0.0536	7.41
SH-28	3.39	784	19.78	0.5195	6.81
P-19	3.84	209	21.19	0.1328	7.60
BG-10	3.97	200	21.55	0.0545	7.70

30 randomized cross-validation cases yielded topologically identical RPs, contradicting the notion of random noise fitting as depicted in Figs. 7a and 7b. The method achieved RMS at the level of local sample variance, suggesting we indeed identified the underlying radiation pattern up to the noise by polarization, measurement, and propeller scattering; seeFig. 7c. However, compared with the results in Fig. 5a, the pattern may resemble the sampling trajectory, suggesting a possible sampling bias. The results still suggest that the model order as high as 28 correctly fits the fine RP. Whereas the fine-resolution RP ground truth measurement is not available, we leave a detailed discussion about model order selection for future work.

VI. CONCLUSION

The paper explored a novel perspective on Radiation Pattern identification and learning. By treating the *whole* UAV as a complex directional antenna system, a learning method was proposed to identify the Radiation Patterns of *both* UAVs after executing a specific, synchronized calibration trajectory. Among different analytical Radiation Pattern models, the Spherical Harmonics emerged as the most promising, predicting signal quality with RMS error as low as $3.6\,\text{dB}$ measurement noise level. We also discussed a potential issue of overfitting in the model. Compared with the literature we are aware of, the paper presents a new, feasible concept for data-driven antenna Radiation Pattern identification in aerial robotic scenarios, which is useful, for example, in pre-mission calibration procedures.

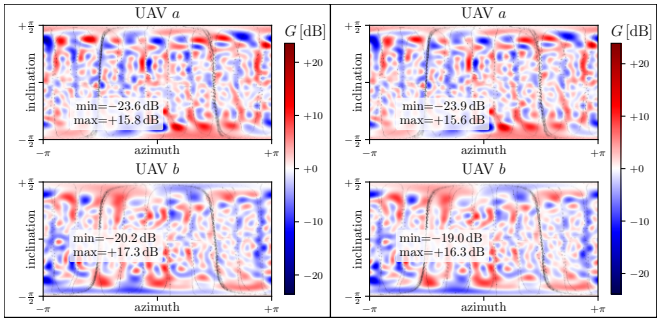

(a) Cross-validation case 1. (b) Cross-validation case 2.

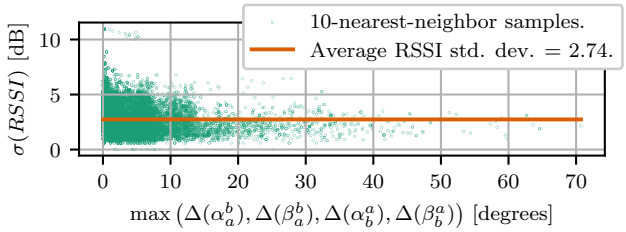

(c) Local noise analysis. Each point represents a statistic of the 10 nearest neighbours of a sample in the dataset. The X-axis denotes the biggest difference among neighbours' features. Most of 10-NN lies within 15°. Y axis denotes the standard deviation of RSSI among the neighbours. The local standard deviation is distributed around 2.74 dB. The noise may come from the rotating propellers of the UAV and polarization mismatch.

Fig. 7. Radiation patterns learnt by Spherical Harmonics (SH), order 28. Two cross-validation instances are depicted. Both patterns are topologically identical, suggesting no overfitting occurred. However, the patterns also resemble sampling paths in Fig. 5, suggesting a sampling bias. Proper analysis of the overfitting is left for future work.

References

[1] J. Diller, J. G. Rogers, N. T. Dantam, and Q. Han, Communication Mapping for Robot Teams, *IEEE Transactions on Field Robotics*, vol. 2. pp. 288307, 2025. DOI: 10.1109/tfr.2025.3568794.

[2] A. Quattrini Li, P. K. Penumarthi, J. Banfi, *et al.*, Multi-robot online sensing strategies for the construction of communication maps, *Autonomous Robots*, vol. 44, no. 34. pp. 299319, 22, 2019. DOI: 10.1007/s10514-019-09862-3.

[3] A. Rizwan, D. Biswas, and V. Ramachandra, Impact of UAV structure on antenna radiation patterns at different frequencies, *2017 IEEE International Conference on Antenna Innovations & Modern Technologies for Ground, Aircraft and Satellite Applications (iAIM)*. pp. 15, 2017. DOI: 10.1109/iaim.2017.8402597.

[4] D. Bonilla Licea, M. Bonilla E., M. Ghogho, and M. Saska, Energy-Efficient Fixed-Wing UAV Relay With Considerations of Airframe Shadowing, *IEEE Communications Letters*, vol. 27, no. 6. pp. 15501554, 2023. DOI: 10.1109/lcomm.2023.3264780.

[5] A. T. Koru, J. Chang, and Y. Wan, RSSI-Based Distributed Control to Align Directional Antenna Pairs for UAV Communication, *IEEE/ASME Transactions on Mechatronics*, vol. 29, no. 4. pp. 28772885, 2024. DOI: 10.1109/tmech.2024.3403911.

[6] D. B. Licea, G. Silano, M. Ghogho, and M. Saska, Communications-Aware Robotics: Challenges and Opportunities, *2023 International Conference on Unmanned Aircraft Systems (ICUAS)*. 06, 2023. DOI: 10.1109/icuas57906.2023.10155882.

[7] A. Muralidharan and Y. Mostofi, Communication-Aware Robotics: Exploiting Motion for Communication, *Annual Review of Control, Robotics, and Autonomous Systems*, vol. 4, no. 1. pp. 115139, 03, 2021. DOI: 10.1146/annurev-control-071420-080708.

[8] M. D. Bedford, A. Hrovat, G. Kennedy, *et al.*, Modeling Microwave Propagation in Natural Caves Using LiDAR and Ray Tracing, *IEEE Transactions on Antennas and Propagation*, vol. 68, no. 5. pp. 38783888, 2020. DOI: 10.1109/tap.2019.2957969.

[9] M. Malmirchegini and Y. Mostofi, On the Spatial Predictability of Communication Channels, *IEEE Transactions on Wireless Communications*, vol. 11, no. 3. pp. 964978, 2012. DOI: 10.1109/twc.2012.012712.101835.

[10] L. Clark, J. Edlund, M. S. Net, *et al.*, PropEM-L: Radio Propagation Environment Modeling and Learning for Communication-Aware Multi-Robot Exploration, *Robotics: Science and Systems XVIII*. 27, 2022. DOI: 10.15607/rss.2022.xviii.014.

[11] Z. Becvar, J. Plachy, P. Mach, *et al.*, Machine Learning for Channel Quality Prediction: From Concept to Experimental Validation, *IEEE Transactions on Wireless Communications*, vol. 23, no. 10. pp. 1460514619, 2024. DOI: 10.1109/twc.2024.3417532.

[12] C. Ge, D. Zhai, Y. Jiang, *et al.*, Pathloss and Airframe Shadowing Loss of Air-to-Ground UAV Channel in the Airport Area at UHF- and L-Band, *IEEE Transactions on Vehicular Technology*, vol. 72, no. 6. pp. 80948098, 2023. DOI: 10.1109/tvt.2023.3242461.

[13] O. Esrafilian, R. Gangula, and D. Gesbert, UAV Trajectory Optimization and Tracking for User Localization in Wireless Networks. 2023. DOI: 10.48550/ARXIV.2305.14959.

[14] G. Pupillo, G. Naldi, G. Bianchi, *et al.*, Medicina array demonstrator: calibration and radiation pattern characterization using a UAV-mounted radio-frequency source, *Experimental Astronomy*, vol. 39, no. 2. pp. 405421, 29, 2015. DOI: 10.1007/s10686-015-9456-z.

[15] M. H. Syed, M. Singh, and J. Camp, Direction Estimation in 3D Outdoor Air-Air Wireless Channels through Machine Learning, *Sensors*, vol. 23, no. 23. p. 9524, 30, 2023. DOI: 10.3390/s23239524.

[16] D. B. Licea, H. El Hammouti, G. Silano, and M. Saska, Harnessing the Potential of Omnidirectional Multi-Rotor Aerial Vehicles in Cooperative Jamming Against Eavesdropping, *GLOBECOM 2024 - 2024 IEEE Global Communications Conference*. pp. 20522058, 08, 2024. DOI: 10.1109/globecom52923.2024.10901802.

[17] D. B. Licea, G. Silano, M. Ghogho, and M. Saska, Omnidirectional Multi-Rotor Aerial Vehicle Pose Optimization: A Novel Approach to Physical Layer Security, *ICASSP 2024 - 2024 IEEE International Conference on Acoustics, Speech and Signal Processing (ICASSP)*. pp. 90219025, 14, 2024. DOI: 10.1109/icassp48485.2024.10447876.

[18] N. C. Matson, S. M. Hashir, S. Song, *et al.*, Effect of Antenna Orientation on the Air-to-Air Channel in Arbitrary 3D Space, *2021 IEEE 22nd International Symposium on a World of Wireless, Mobile and Multimedia Networks (WoWMoM)*. pp. 298303, 2021. DOI: 10.1109/wowmom51794.2021.00055.

[19] M. Rahman, I. Guvenc, J. A. Abrahamson, *et al.*, Characterization of the Combined Effective Radiation Pattern of UAV-Mounted Antennas and Ground Station. 2025. DOI: 10.48550/ARXIV.2506.01925.

[20] M. Badi, J. Wensowitch, D. Rajan, and J. Camp, Experimentally Analyzing Diverse Antenna Placements and Orientations for UAV Communications, *IEEE Transactions on Vehicular Technology*, vol. 69, no. 12. pp. 1498915004, 2020. DOI: 10.1109/tvt.2020.3031872.

[21] B. Hu and X. Dong, Communications Channel Characteristics in the Presence of Aircraft Body Blockage in Urban Air Mobility, *IEEE Transactions on Vehicular Technology*, vol. 73, no. 7. pp. 1070310707, 2024. DOI: 10.1109/tvt.2024.3384375.

[22] S. Jan, Y. Liu, and C. D. Sarris, Efficient Neural Network-Based Reconstruction of Three-Dimensional Antenna Radiation Patterns From Two-Dimensional Cuts, *IEEE Open Journal of Antennas and Propagation*, vol. 6, no. 3. pp. 726734, 2025. DOI: 10.1109/ojap.2025.3544968.

[23] J. Wang and Y. Rahmat-Samii, New Cosine-q Pattern Formulas for the Analysis of Elongated-Aperture Antennas, *IEEE Transactions on Antennas and Propagation*, vol. 72, no. 2. pp. 18931898, 2024. DOI: 10.1109/tap.2023.3348573.

[24] E. K. Miller, Adaptive Sparse Sampling to Estimate Radiation and Scattering Patterns to a Specified Uncertainty with Model-Based Parameter Estimation: Compute patterns using as few as two to four samples per lobe, *IEEE Antennas and Propagation Magazine*, vol. 57, no. 4. pp. 103113, 2015. DOI: 10.1109/map.2015.2453920.

[25] J. Chen, D. Raye, W. Khawaja, *et al.*, Impact of 3D UWB Antenna Radiation Pattern on Air-to-Ground Drone Connectivity, *2018 IEEE 88th Vehicular Technology Conference (VTC-Fall)*. pp. 15, 2018. DOI: 10.1109/vtcfall.2018.8690726.

[26] D. Bonilla Licea, M. Ghogho, and M. Saska, When Robotics Meets Wireless Communications: An Introductory Tutorial, *Proceedings of the IEEE*, vol. 112, no. 2. pp. 140177, 2024. DOI: 10.1109/jproc.2024.3380373.

[27] A. Schmitz, T. Karolski, and L. Kobbelt, Using spherical harmonics for modeling antenna patterns, *2012 IEEE Radio and Wireless Symposium*. pp. 155158, 2012. DOI: 10.1109/rws.2012.6175298.